

ASTROPHYSICAL IMPACT OF THE UPDATED ${}^9\text{Be}(p,\alpha){}^6\text{Li}$ AND ${}^{10}\text{B}(p,\alpha){}^7\text{Be}$ REACTION RATES AS DEDUCED BY THM

L. LAMIA¹, C. SPITALERI^{1,2}, E. TOGNETTI^{3,4}, S. DEGL'INNOCENTI^{3,5}, R. G. PIZZONE², AND P. G. PRADA MORONI^{3,5}

¹Department of Physics and Astronomy, University of Catania, Catania, Italy

²INFN—Laboratori Nazionali del Sud, Catania, Italy

³INFN, Section of Pisa, Largo Bruno Pontecorvo 3, I-56127, Pisa, Italy

⁴Department of Physics, University of Roma Tor Vergata, Via della Ricerca Scientifica 1, I-00133, Roma, Italy

⁵Department of Physics “E. Fermi,” University of Pisa, Largo Bruno Pontecorvo 3, I-56127, Pisa, Italy

Received 2015 May 15; accepted 2015 July 24; published 2015 September 28

ABSTRACT

The complete understanding of the stellar abundances of lithium, beryllium, and boron represents one of the most interesting open problems in astrophysics. These elements are largely used to probe stellar structure and mixing phenomena in different astrophysical scenarios, such as pre-main-sequence or main-sequence stars. Their different fragility against (p,α) burning reactions allows one to investigate different depths of the stellar interior. Such fusion mechanisms are triggered at temperatures between $T \approx (2\text{--}5) \times 10^6$ K, thus defining a corresponding Gamow energy between $\approx 3\text{--}10$ keV, where $S(E)$ -factor measurements need to be performed to get reliable reaction rate evaluations. The Trojan Horse Method is a well defined procedure to measure cross sections at Gamow energies overcoming the uncertainties due to low-energy $S(E)$ -factor extrapolation as well as electron screening effects. Taking advantage of the THM measure of the ${}^9\text{Be}(p,\alpha){}^6\text{Li}$ and ${}^{10}\text{B}(p,\alpha){}^7\text{Be}$ cross sections, the corresponding reaction rates have been calculated and compared with the evaluations by the NACRE collaboration, widely used in the literature. The impact on surface abundances of the updated ${}^9\text{Be}$ and ${}^{10}\text{B}$ (p,α) burning rates is discussed for pre-MS stars.

Key words: nuclear reactions, nucleosynthesis, abundances – stars: abundances – stars: evolution – stars: pre-main sequence

1. INTRODUCTION

The light elements lithium, beryllium, and boron experience nuclear burning at stellar depths where temperatures of a few 10^6 K are reached, ranging from $T \approx 2 \times 10^6$ K for ${}^6\text{Li}$ to $T \approx (4\text{--}5) \times 10^6$ K for boron isotopes. Thus, their surface abundances are strongly influenced by the nuclear burnings as well as by the extension of the convective envelope (see, e.g., Deliyannis et al. 2000; Jeffries 2006). Indeed, in convective regions the matter is completely mixed, and if the burning temperature is reached at least at the bottom of the convective envelope, the element abundance decreases on the surface too. In addition, the extension of the convective envelope has an opposite dependence on stellar age, mass, and chemical composition with respect to the one of the stellar temperature. In more detail, while for a fixed point of the stellar interior, the temperature increases with the mass, age, and original helium abundance, for the same variations the external convective region gets shallower; moreover, the temperature decreases, increasing the stellar metallicity while the convective envelope gets deeper (see, e.g., Jeffries et al. 2000; Dotter et al. 2008; Di Criscienzo et al. 2009, and references therein). This leads to a complex dependence of surface abundances on stellar mass, chemical composition, and age.

Pre-main-sequence (pre-MS) stars show deep convective envelopes at the bottom of which light element ignition temperatures can be reached (depending on the mass), while during the following main-sequence (MS) phase convective envelopes are shallower and light element burning is less favorable, although it could still be triggered depending on the element and on the stellar characteristics.

The prediction of surface abundances for lithium, beryllium, and boron in stars still represents an unsolved and challenging

task for astrophysics since they strongly depend on the adopted input physics in theoretical models (e.g., nuclear reaction rates, opacity of the stellar matter, equation of state, efficiency of microscopic diffusion, etc., see, e.g., Piau & Turck-Chièze 2002; D’Antona & Montalbán 2003; Montalbán & D’Antona 2006; Tognelli et al. 2012) as well as on the assumed external convection efficiency. The difficulty in calculating these stellar abundances is proven, for example, by the still present discrepancy between theoretical predictions and observational ${}^7\text{Li}$ data (the so-called “lithium-problem,” see, e.g., Charbonnel et al. 2000; Deliyannis et al. 2000; Pinsonneault et al. 2000; Baraffe & Chabrier 2010; Talon & Charbonnel 2010).

Besides lithium, remarkable efforts have also been made for studying beryllium and boron stellar abundances. Indeed, the comparison between theory and observation for Be and B surface abundances could provide useful additional information. In particular, ${}^9\text{Be}$ is burnt at temperatures higher than the ${}^7\text{Li}$ ones ($T \approx 3.5 \times 10^6$ K to be compared with $T \approx 2.5 \times 10^6$ K for ${}^7\text{Li}$) thus simultaneous observations of ${}^7\text{Li}$ and ${}^9\text{Be}$ could constrain theoretical models with particular regard to the extension of the convective envelope.

Unluckily, spectroscopic ${}^9\text{Be}$ abundance determinations mainly rely on resonance lines located in the near-UV spectral region of cool stars, whose observation from ground-based telescopes is very difficult. The bulk of observations is for metallicities near to the solar one, even if data are available in a much wider range of chemical compositions.

Up to now, ${}^9\text{Be}$ can be safely measured only in stars with temperatures higher than about 5000–5200 K (see, e.g., Garcia Lopez et al. 1995; Randich et al. 2007; Smiljanic et al. 2011; Delgado Mena et al. 2012). In agreement with theoretical predictions, these stars do not show any pre-MS ${}^9\text{Be}$ surface

depletion and thus they are only marginally useful to further constrain convection efficiency during this evolutionary phase (see, e.g., Smiljanic et al. 2011). On the contrary, smaller stars with a deeper and hotter bottom of the convective envelope, are expected to burn ${}^9\text{Be}$ in pre-MS, thus representing a more useful benchmark for testing convective models.

The solar photospheric ${}^9\text{Be}$ abundance has been largely investigated in the past. In an early analysis (see, e.g., Chmielewski et al. 1975), a relatively large discrepancy between the meteoric (protosolar) and the solar ${}^9\text{Be}$ abundance emerged, in which the solar was smaller by a factor 1.8 with respect to the protosolar one. This discrepancy opened a debate about a possible degree of ${}^9\text{Be}$ depletion in the Sun, though not predicted by theoretical models, and consequently raised the quest for additional non-standard depletion mechanisms. However, the more recent observations and accurate solar spectra analysis lead to a revised higher solar ${}^9\text{Be}$ abundance (Balachandran & Bell 1998; Lodders 2003; Asplund et al. 2005, 2009; Lodders et al. 2009; Lodders 2010), fully consistent with the meteoric one, solving the long-standing problem of the solar ${}^9\text{Be}$.

Concerning the models, theoretical expectations for solar mass stars predict no surface ${}^9\text{Be}$ depletion during the pre-MS nor during the MS phase, in agreement with data. For less massive mid-aged stars (with an effective temperature of $T_{\text{eff}} \lesssim 5600$ K), observations reveal an increasing ${}^9\text{Be}$ depletion while T_{eff} decreases, in disagreement with standard theoretical calculations (no significant rotation effects, no magnetic fields, etc., see, e.g., Santos et al. 2004; Randich et al. 2007; Delgado Mena et al. 2012). Such a depletion, which has not yet been seen in young clusters (e.g., Smiljanic et al. 2011), seems to indicate a possible cause acting on the MS timescale. The level of discrepancy between predictions and observations, or the difference between surface Be abundance in depleted and undepleted stars is significantly larger than observational uncertainties and even larger than the initial ${}^9\text{Be}$ abundances (solar or meteoritic) adopted by different authors. We note that the inclusion in stellar calculations of non-standard processes acting on MS timescales (such as rotation induced mixing, internal waves mixing, internal magnetic fields, etc.) allows us to better reproduce some of the ${}^9\text{Be}$ (and ${}^7\text{Li}$) observational features, thus partially alleviating the discrepancy (see, e.g., Montalbán & Schatzman 2000; Talon & Charbonnel 2010, and references therein).

Similarly to the ${}^9\text{Be}$, solar boron abundance showed a large discrepancy between the meteoric and the photospheric determinations. However, as for ${}^9\text{Be}$, more recent analysis of the solar spectrum have restored the agreement with the meteoric value (Asplund et al. 2009; Lodders 2010).

The spectroscopic measurements of surface ${}^{10,11}\text{B}$ isotopes abundance are even more problematic than the ${}^9\text{Be}$ one. Boron can only be measured from transitions that fall mainly in the ultraviolet, out of the Earth's UV transmission limit. Its abundance can be obtained from neutral boron in cool stars and from ionized boron in high mass stars (spectral types A and B). Moreover, for disk metallicity stars, the neutral boron transition region is affected by strong blending problems (see, e.g., Cunha 2010; Kaufer et al. 2010). In the observed stars, the ratio ${}^{11}\text{B}/{}^{10}\text{B}$ seems to be of the order of four, in agreement with solar values and meteorite results, even if it is very difficult to spectroscopically discriminate among the boron isotopes (see,

e.g., Chaussidon & Robert 1995; Lambert et al. 1998; Rebull et al. 1998; Proffitt & Quigley 1999; Prantzos 2012).

The ${}^{10,11}\text{B}$ -burning temperature is the highest (about $(4-5) \times 10^6$ K) among light elements, thus standard stellar models predict that only masses lower than about $0.5 M_{\odot}$ show surface boron depletion. Cool stars with masses near the solar one with no ${}^9\text{Be}$ depletion appear boron undepleted too, in agreement with the results for the Sun (Boesgaard et al. 2005; Lodders et al. 2009). To observe ${}^{10,11}\text{B}$ depletion, lower masses are needed. However, some F and G MS stars with ${}^9\text{Be}$ depletion seem to show slight B depletion as well, in disagreement with standard stellar model predictions (see, e.g., Boesgaard et al. 2005), but the observational difficulties prevent any firm conclusions.

In the present work, due to the discussed observational problems and the difficulty to consistently reproduce the MS observational data, we decided to restrict our analysis of ${}^9\text{Be}$ and ${}^{10}\text{B}$ abundances to the pre-MS evolution of low-mass stars (i.e., $M \lesssim 1.0 M_{\odot}$).

For a better understanding of this complex scenario, stellar models need to be computed by using input physics that are as accurate as possible. Indeed, it has been shown in several works that pre-MS evolutionary models and, in particular, the surface abundance of light elements (i.e., Li, Be, B) are quite sensitive to both the input physics (i.e., outer boundary conditions, convection, equation of state, reaction rates, opacity, etc.) and/or chemical element abundances (i.e., initial abundance of deuterium, helium, metals, etc.) adopted in stellar models (see, e.g., Burrows et al. 2001; Piau & Turck-Chièze 2002; Burke et al. 2004; Tognelli et al. 2012, 2015b). In this paper, we only focus on the burning nuclear reaction cross sections for ${}^9\text{Be}$ and ${}^{10}\text{B}$, taking advantage of the recent measurements performed via the indirect Trojan Horse Method (THM; Spitaleri et al. 2011; Tribble et al. 2014). We assumed that the other input physics along with the chemical composition are fixed, thus we have performed a differential analysis of the impact of the updated ${}^9\text{Be}$ and ${}^{10}\text{B}$ reaction rates on the ${}^9\text{Be}$ and ${}^{10}\text{B}$ surface abundances in pre-MS stars for different masses.

The nuclear burning reaction rates, in fact, constitute key ingredients for light element surface abundance predictions, and they require particular effort in measuring their values in terrestrial laboratories. In the case of charged-particle induced reactions and because, for quiescent burning, the corresponding Gamow peak usually lies in the *keV*-*s-regime*, direct measurements in laboratories need to be performed at such energies or close to these, as much as possible. However, the presence of the Coulomb barrier among the interacting nuclei cause an exponential drop of the cross-section to nano-or-picobarn values in correspondence of the astrophysical relevant energies, thus often making their measurements impossible and leaving *extrapolations* as the most common means of determining their values. Usually, extrapolation procedures are performed on the astrophysical $S(E)$ -factor, defined as

$$S(E) = E \times \sigma(E) \times \exp(2\pi\eta) \quad (1)$$

for which a more smooth variation with the energy is expected for non-resonant reactions (Rolfs & Rodney 1988). However, it has been shown that experimental $S(E)$ -factor determinations suffer, at astrophysical energies, the presence of electron screening effects for which the “bare-nucleus” cross section is altered by an empirical enhancing factor f_{enh} given in the

laboratory by (Assenbaum et al. 1987; Strieder et al. 2001)

$$f_{\text{enh}} = \frac{S(E)_{\text{sh}}}{S(E)_{\text{b}}} = \frac{\sigma(E)_{\text{sh}}}{\sigma(E)_{\text{b}}} \approx \exp\left(\pi\eta\frac{U_e}{E}\right), \quad (2)$$

where σ_{sh} is the *shielded* nuclear cross section measured in the laboratory, σ_{b} is the *bare-nucleus* cross section, and U_e is the electron screening potential measured in the laboratory.

The direct measurement of the ${}^9\text{Be}(p,\alpha){}^6\text{Li}$ is discussed in Sierk & Tombrello (1973), where the authors report the measurement of both (p, α) and (p,d) channel from 400 keV down to ~ 100 keV, giving a total value of $S(0) = 35^{+45}_{-15}$ MeV b. From their extrapolation at lower energies, one can obtain a value of $S(0) \sim 17$ MeV b for the ${}^9\text{Be}(p,\alpha){}^6\text{Li}$ reaction. Additionally, in the work of Zahnw et al. (1997), the authors explored the low-energy region down to ~ 16 keV extracting the value of $U_e = 900 \pm 50$ eV for the electron screening potential.

In the case of the ${}^{10}\text{B}(p,\alpha){}^7\text{Be}$ reaction, the low-energy region (i.e., below ~ 100 keV), is dominated by the 8.699 MeV ${}^{11}\text{C}$ excited level intervening as an s-wave resonance at about 10 keV in the ${}^{10}\text{B}$ -p center of mass system, as discussed in detail in Angulo et al. (1993). By describing their experimental data, assuming the same enhancing electron screening potential of 430 ± 50 eV measured by the ${}^{11}\text{B}$ -p interaction, the authors extrapolated a value of $S(10 \text{ keV}) = 2870 \pm 500$ MeV b.

In order to complement the already available $S(E)$ -factor direct measurements, and to bypass extrapolation procedures at low-energies (i.e., below ~ 100 keV's), the previous reactions have additionally been studied by means of the Trojan Horse Method (THM). The method, for which reviews can be found in Spitaleri et al. (2011) and Tribble et al. (2014), allows the experimentalist to bypass the typical difficulties of direct approaches, such as the presence of the Coulomb barrier in the entrance channel or the presence of the electron screening phenomena. Due to its theoretical formalism, THM data need to be normalized to high-energy direct data in which either Coulomb penetrability or electron screening effects are negligible. Thus, THM acts as a complementary experimental technique for nuclear astrophysics. Thanks to its development in the last ~ 25 years, THM have been used in investigating the above mentioned reactions of interest here.

The ${}^9\text{Be}(p,\alpha){}^6\text{Li}$ reaction has been studied in the works of Romano et al. (2006) and of Wen et al. (2008) by properly selecting the quasi-free (QF) contribution of the ${}^2\text{H}({}^9\text{Be}, \alpha^6\text{Li})\text{n}$ reaction in two different experiments. The THM measurements lead to a zero-energy $S(E)$ -factor of $S(0) = 21.0 \pm 0.8$ (MeV b) and an electron screening potential of $U_e = 676 \pm 86$ eV.

The ${}^{10}\text{B}(p,\alpha){}^7\text{Be}$ has been studied in the work of Lamia et al. (2007) and recently in Spitaleri et al. (2014), in order to measure the corresponding $S(E)$ -factor value by means of THM applied to the QF reaction ${}^2\text{H}({}^{10}\text{B}, \alpha^7\text{Be})\text{n}$. The investigation allowed us to measure the $S(E)$ -factor in correspondence with the Gamow energy region in which the 8.701 MeV level of ${}^{11}\text{C}$ intervenes as an $l = 0$ resonance at ~ 10 keV dominating the whole excitation function from ~ 100 keV's down to zero. The $S(E)$ -factor values measured are $S(10 \text{ keV}) = 3127 \pm 583$ (MeV b) and $U_e = 240 \pm 200$ eV, with this last value being strongly affected by the still present uncertainties on direct measurements at which THM data have been normalized (see the discussion in Spitaleri et al. 2014).

In this paper, the ${}^9\text{Be}$ and ${}^{10}\text{B}$ (p, α) burning reaction rates have been evaluated by means of the THM cross-section

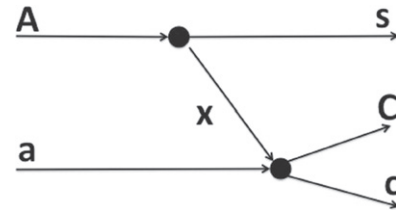


Figure 1. Schematic representation of the quasi-free (QF) $a + A \rightarrow c + C + s$ reaction via the pole diagram as in Shapiro (1967). The TH nucleus A breaks up into x and s , which are called the *participant* and the *spectator* of the binary $a(x, c)C$ reaction, respectively.

measurements listed above. These were then compared with the widely used NACRE reaction rates (Angulo et al. 1999) and with the more recent NACREII compilation (Xu et al. 2013). The impact of the updated ${}^9\text{Be}$ and ${}^{10}\text{B}$ burning reaction rates on the ${}^9\text{Be}$ and ${}^{10}\text{B}$ surface abundances in pre-MS stars is also discussed.

The paper is organized in the following way. In Section 2, we briefly recall the main characteristics of the THM method, then we discuss the results of the ${}^9\text{Be}$ and ${}^{10}\text{B}$ cross-section measurements in Section 3. In Section 4, we derive an analytical expression of the quoted reaction rates to be directly incorporated in the stellar evolutionary code. In Section 5, we present the stellar models and discuss the effects on stellar surface abundances of the adoption of new ${}^9\text{Be}$ and ${}^{10}\text{B}$ THM reaction rates. We summarize the main results in Section 6.

2. THE THM

To by-pass extrapolation procedure and systematic uncertainties due to electron screening effects, the indirect method of the Trojan Horse (Baur 1986; Spitaleri 1990; Cherubini et al. 1996; Spitaleri et al. 1999, 2011; Tribble et al. 2014) has been developed and largely used in the past to shed light on different open issues concerning both pure nuclear physics and nuclear astrophysics.

Indeed, THM allows experimentalists to measure the astrophysically relevant cross sections in correspondence, or very close, to the so-called Gamow peak without experiencing the lowering of the signal-to-noise ratio due to the presence of the Coulomb barrier between the interacting particles.

By referring to the pole diagram of Figure 1, THM selects the QF contribution of the $a + A \rightarrow c + C + s$ reaction, where the Trojan nucleus A is chosen because of its large amplitude for the $A = x \oplus s$ cluster configuration. The $a + A$ interaction occurs at energies well above the Coulomb barrier, for extracting the bare nucleus cross section of the astrophysically relevant reaction $a + x \rightarrow c + C$ at low-energies, without the action of both Coulomb suppression or electron screening effects (see Spitaleri et al. 2011; Tribble et al. 2014, for more details). In the pole diagram of Figure 1, particle a will then interact only with the cluster x of the TH nucleus A , while s will act as spectator to the $A(x, c)C$ virtual reaction. By invoking the more simple plane wave impulse approximation, the cross section of the $A(a, cC)s$ reaction can be factorized into two terms corresponding to the poles of Figure 1 via the formula (Spitaleri et al. 2011; Tribble et al. 2014)

$$\frac{d^3\sigma}{dE_c d\Omega_c d\Omega_C} \propto \text{KF} \cdot |\Phi(\mathbf{p}_{sx})|^2 \cdot \left. \frac{d\sigma}{d\Omega} \right|_{\text{cm}}^{\text{HOES}}, \quad (3)$$

where

1. KF represents the kinematical factor, depending on masses, momenta, and angles of the outgoing particles, that takes into account the final state phase space factor;
2. $|\Phi(\mathbf{p}_{xs})|^2$ is given by the Fourier transform of the radial wave function describing the $x-s$ inter-cluster motion, usually in terms of Hänkel, Eckart, or Hulthén functions depending on the $x-s$ system;
3. $d\sigma/d\Omega|_{\text{cm}}^{\text{HOES}}$ is the half-off-energy-shell (HOES) differential cross section for the two-body reaction at the center of mass energy $E_{\text{cm}} = E_{cc} - Q$, where Q represents the Q -value of the virtual $A(x, c)C$ reaction, while E_{cc} represents the relative $c-C$ energy measured in the laboratory.

The introduction of the penetration factor through the Coulomb barrier, described in terms of the regular and irregular Coulomb functions, and the normalization to the high-energy direct measurements, make the extraction of the bare-nucleus $S(E)$ -factor possible by following Equation (1), where the THM cross section represents the bare nucleus one.

In recent years, THM data allowed for a better understanding of different astrophysical problems, such as the study of light element burning reactions (Pizzone et al. 2005, 2014; Lamia et al. 2008, 2012b, 2012c, 2013; Tumino et al. 2011a, 2011b, 2014; Grineviciute et al. 2015), CNO reactions (see La Cognata et al. 2010, 2011; Sergi et al. 2010; Palmerini et al. 2013), and removing/producing neutron reactions (Lamia et al. 2008; Gulino et al. 2010, 2013; La Cognata et al. 2012).

3. LIGHT ELEMENT BURNING REACTIONS AS EXPLORED VIA THM

The light elements lithium, beryllium, and boron (p, α) burning reactions have been largely investigated by THM in order to access the Gamow energy, known by direct measurements only via extrapolation procedures. Here, the main results obtained are briefly reported.

3.1. The ${}^9\text{Be}(p, \alpha){}^6\text{Li}$ Reaction

The first THM measurement of the ${}^9\text{Be}(p, \alpha){}^6\text{Li}$ $S(E)$ -factor has been performed in Romano et al. (2006), by properly selecting the QF-contribution of the three-body reaction ${}^2\text{H}({}^9\text{Be}, \alpha){}^6\text{Li}n$ with a devoted experiment performed at INFN-LNS of Catania, in which a 22 MeV ${}^9\text{Be}$ beam hit a $190 \mu\text{g cm}^{-2}$ thick CD_2 target. In such a framework, deuterium ${}^2\text{H}$ has been used as the “TH-nucleus” because of its obvious p - n structure and the relative p - n motion, mainly occurring in s -wave (Lamia et al. 2012a). The transferred proton p and neutron n represent the *participant* and the *spectator*, respectively, in agreement with the sketch of Figure 1. The detection setup consisted of a standard ΔE - E telescope, with a position sensitive silicon detector (PSD) as E -stadium, working in logic coincidence with a further PSD detector, placed on the opposite side with respect to the beam axis, as discussed in Romano et al. (2006). The measurement of Romano et al. (2006) allowed for the first time the extraction of the angular distributions at different energies and the investigation of the low-lying resonance at ~ 250 keV. Thanks to both experimental and theoretical improvements concerning the method, a second experiment has been performed at the China Institute of Atomic Energy, Beijing, China, and the results reported in Wen et al.

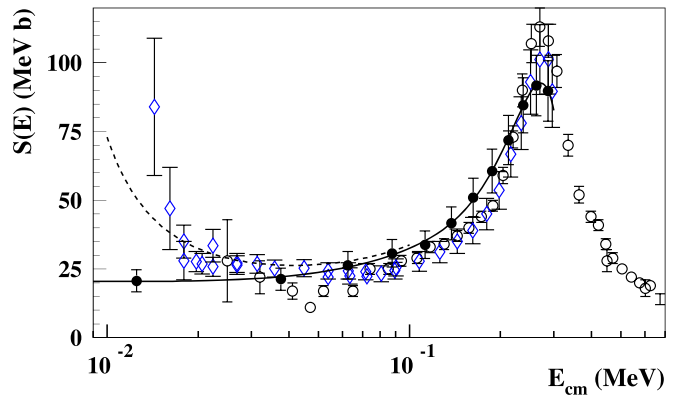


Figure 2. THM ${}^9\text{Be}(p, \alpha){}^6\text{Li}$ $S(E)$ -factor (black-points) compared to the direct data as reported in the NACRE compilation. The direct data of Zahnov et al. (1997) have also been used for extracting the electron screening potential U_e . The full black line describes the fit of the bare nucleus THM data, leading to $S(0) = 21.0 \pm 0.8$ (MeV b). The dashed line describes the enhancing caused by electron screening effects with a fitted value of $U_e = 676 \pm 86$ eV, as given in Wen et al. (2008).

(2008), of the detailed analysis of the QF-mechanism selection and background discrimination are discussed. The experimental THM data have then been normalized to the direct ones available in the NACRE compilation, thus allowing for a polynomial fit from ~ 100 keV’s down to zero as (see Wen et al. 2008)

$$S(E) = 21.0 - 92.4 \times E + 4669 \times E^2 - 4.4 \times 10^4 \times E^3 + 2.2 \times 10^5 \times E^4 - 3.8 \times 10^5 \times E^5, \quad (4)$$

where E represents the center-of-mass energy in the ${}^9\text{Be}-p$ system, expressed in MeV. Equation (4) leads to the values of $S(0) = 21.0 \pm 0.8$ (MeV b) and $U_e = 676 \pm 86$ eV, respectively, for the $S(0)$ and U_e values. Since the *measured* THM zero-energy $S(E)$ -factor deviates from the low-energy *extrapolation* of NACRE by a factor of ~ 1.23 , the corresponding reaction rate evaluation needs to be performed to study its impact on astrophysical scenarios where beryllium is destroyed, such as the pre-MS evolution of low-mass stars.

3.2. The ${}^{10}\text{B}(p, \alpha){}^7\text{Be}$ reaction

The study of the ${}^{10}\text{B}(p, \alpha){}^7\text{Be}$ reaction is of importance in nuclear astrophysics because of the difficulty in measuring the corresponding $S(E)$ -factor at Gamow energies and the astrophysical community’s interest in the production/destroying processes of the unstable ${}^7\text{Be}$ isotope (see, for instance, Simonucci et al. 2013). Indeed, the 8.701 MeV excited level of ${}^{11}\text{C}$ dominates the $S(E)$ -factor trend at low-energies, being this an s -wave resonance in the ${}^{10}\text{B}-p$ system at 10 keV. However, due to the action of both Coulomb barrier and electron screening effects, the $S(10 \text{ keV})$ -factor was only extrapolated from the high energy measurement (Angulo et al. 1999). To bypass extrapolations, a first THM measurement has been discussed in Lamia et al. (2007), where the dominance of the QF reaction mechanism intervening in the ${}^2\text{H}({}^{10}\text{B}, \alpha){}^7\text{Be}n$ has been constrained via the study of the experimental momentum distribution. The work reports on the ${}^2\text{H}({}^{10}\text{B}, \alpha){}^7\text{Be}n$ experiment performed at USP (University of Sao Paulo, Brazil) by means of a 24 MeV ${}^{10}\text{B}$ beam hitting a $190 \mu\text{g cm}^{-2}$ thick

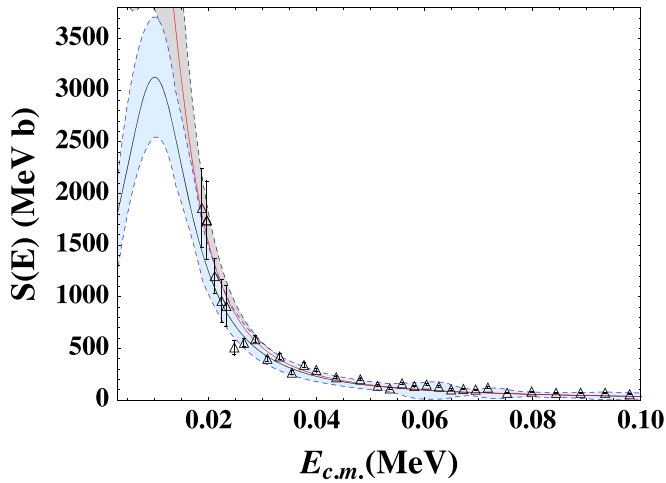


Figure 3. THM $^{10}\text{B}(p,\alpha)^7\text{Be}$ $S(E)$ -factor (full blue line) compared with the direct data as reported in the NACRE compilation (empty points with their errors). The full red line describes the enhancing of the direct data of Angulo et al. (1993) due to electron screening phenomena Spitaleri et al. (2014).

CD_2 target. The adopted detection setup allowed for ^7Be identification and alpha-particle detection, as described in Lamia et al. (2007). The experiment has made it possible to detect the population of the ~ 10 keV resonance intervening in the ^{10}B -p center-of-mass system, although the limited energy resolution (of about ~ 60 keV) did not allow us to get any definitive results. A further experimental run has been performed at INFN-LNS (INFN-Laboratori Nazionali del Sud, Catania, Italy) with the aim of enhancing the energy resolution and constraining the $S(10 \text{ keV})$ -factor. Thanks to the available CAMERA2000 scattering chamber, a very extreme angular resolution has been obtained (i.e., of about $0^\circ.1$), which is a key requirement for THM purposes as deeply discussed in the paper of Spitaleri et al. (2011). The INFN-LNS measurement allowed us, at the end, to reach an overall energy resolution of ~ 16 keV. The complete analysis of the experiment, together with a detailed DWBA calculation for the momentum distribution made with the FRESCO code and the proposed R -matrix calculation, are deeply discussed in Spitaleri et al. (2014). The THM experimental data have been folded for the experimental resolution and normalized to the available direct data of Angulo et al. (1993) in the center of mass energy region ranging from 60 keV up to 100 keV. Thus, following the procedure described in Spitaleri et al. (2014), the experimental data have been fitted by means of a standard Breit–Wigner function centered at 10 keV and with a total width of $\Gamma = 15$ keV (as reported in Angulo et al. 1993) superimposed on a non-resonant contribution, thus leading to the value of $S(10 \text{ keV}) = 3127 \pm 583$ (MeV b) in correspondence with the resonance energy. The result of such an analysis is summarized in Figure 3, where the empty triangles are the direct data of Angulo et al. (1993), while the full black line represents the THM bare-nucleus $S(E)$ -factor at “infinite resolution.” Its uncertainties are represented by the blue area. By using this measured THM $S(E)$ -factor, the low-energy direct data (i.e., $E_{\text{cm}} < 40$ keV) have been fitted by means of the enhancing factor given in Equation 2 with an electron screening potential of $U_e = 240 \pm 200$ eV. The result of such a fit is represented by the red-line of Figure 3 while the gray area marks the corresponding uncertainties.

Table 1
Reaction Rate Parameters Intervening in Equation (5) for the $^9\text{Be}(p,\alpha)^6\text{Li}$ and $^{10}\text{B}(p,\alpha)^7\text{Be}$ Studied Via the THM

Parameter a_i	$^9\text{Be}(p,\alpha)^6\text{Li}$	$^{10}\text{B}(p,\alpha)^7\text{Be}$
a_1	3.67985×10^1	-9.19899×10^1
a_2	-7.50748×10^{-4}	1.64250×10^{-2}
a_3	-9.70728	-2.40164×10^1
a_4	-1.90475×10^1	1.81265×10^2
a_5	2.60169×10^1	-9.26607×10^1
a_6	-2.57245×10^1	4.45586×10^1
a_7	1.41609	-3.07591×10^1

Note. THM reaction rates are valid for $T_9 < 0.2$.

4. REACTION RATE CALCULATION AND PARAMETRIZATION

Starting from the THM experiment discussed above, the reaction rate at astrophysical energies has been deduced via the standard formula given in Rolfs & Rodney (1988)

$$N_A \langle \sigma v \rangle = \left(\frac{8}{\pi \mu} \right)^{\frac{1}{2}} \frac{N_A}{k T_9^{\frac{3}{2}}} \int_0^\infty S_b(E) e^{-2\pi\eta - \frac{E}{kT}} dE \quad (\text{cm}^3 \text{mol}^{-1} \text{s}^{-1}), \quad (5)$$

where the temperature T_9 is expressed in units of 10^9 K and the center of mass energy E in MeV. In Equation (5), the bare-nucleus $S(E)$ -factor, $S_b(E)$, is the one measured at the Gamow energies via the THM and discussed in the previous sections. The integration has been performed through the energy intervals covered by each experiment, i.e., from ~ 200 keV down to about ~ 10 keV, depending on the involved reaction. Thus, the reaction rate has been fitted via the following formula:

$$N_A \langle \sigma v \rangle = \exp \left[a_1 + \frac{a_2}{T_9} + \frac{a_3}{T_9^{1/3}} + a_4 \times T_9^{1/3} + a_5 \times T_9 + a_6 \times T_9^{5/3} + a_7 \times \ln T_9 \right], \quad (6)$$

where the a_i coefficients have been left as free parameters for the two $^9\text{Be}(p,\alpha)^6\text{Li}$ and $^{10}\text{B}(p,\alpha)^7\text{Be}$ reactions. In Equation (6), the temperature T_9 is expressed in units of 10^9 K and the final reaction rate is given in $(\text{cm}^3 \text{mol}^{-1} \text{s}^{-1})$. The resulting a_i coefficients are listed in Table 1. Figure 4 reports the discrepancy in percentage between the calculated THM reaction rate and its parametrization via Equation (6) for the $^9\text{Be}(p,\alpha)^6\text{Li}$ case, leading to a maximum variation of $\pm 0.6\%$ at temperatures $T_9 < 0.2$ thus confirming the goodness of the adopted procedure.

The deduced THM reaction rates, together with the corresponding uncertainties, have been compared to the ones given in the literature with the aim of evaluating the deviation caused by the present THM investigation. In particular, we compared our results with the NACRE compilation, largely used for astrophysical purposes, and with the more recent NACRE II compilation by Xu et al. (2013), in which a comprehensive Distorted Wave Born Approximation (DWBA) calculation has been performed by including all of the measurements “post-NACRE.” Here, we are interested in evaluating the impact of

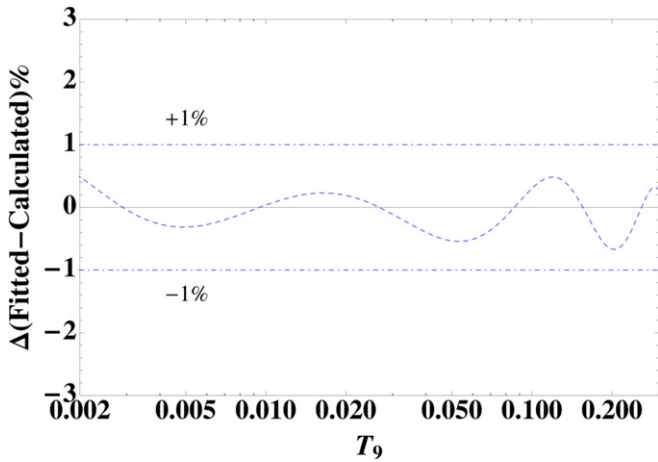


Figure 4. Discrepancy (in percentage) between the calculated and the parametrized THM reaction rate (dashed blue line) for the ${}^9\text{Be}(p,\alpha){}^6\text{Li}$ reaction. The dotted-dashed lines mark the $\pm 1\%$ discrepancy level.

nuclear inputs in the astrophysical scenario by only using the THM bare-nucleus measurements at astrophysical energies.

Figure 5 reports the THM-to-NACRE ratio, i.e.,

$$\frac{N_A \langle \sigma v \rangle_{\text{THM}}}{N_A \langle \sigma v \rangle_{\text{NACRE}}} \quad (7)$$

for the ${}^9\text{Be}(p,\alpha){}^6\text{Li}$ case. The THM reaction rate has been evaluated by considering the $S(E)_b$ -factor given by Equation (4) while the Angulo et al. (1999) compilation adopts the low-energy extrapolation leading to $S(0) = 17^{+25}_{-7}$ MeV b. In Figure 5, the blue line is the ratio between the adopted THM and NACRE reaction rates while the filled red area refers to the range values allowed by the experimental errors on $S(E)$ -measurements given in Wen et al. (2008) and shown in Figure 2. From the present reaction rate determination, a strong reduction of the uncertainties on the reaction rate is clearly visible. In particular, at temperatures lower than 10^8 K, the THM allows us to reduced the reaction rate uncertainties to about $\sim 20\%$, while the NACRE one is given with an uncertainty of $\sim 70\% - 90\%$ at the same temperatures. By also comparing the THM reaction rate extracted here with that given in the NACREII compilation, a reduction of the uncertainty region is clearly visible from Figure 6 while the ratio between the adopted values does not show any significant deviation. This is not unexpected since in the comprehensive fit of Xu et al. (2013) and the THM data of Wen et al. (2008) have been also included, thus dominating the low-energies $S(E)$ -factor data set.

By following the same procedure, the THM ${}^{10}\text{B}(p,\alpha){}^7\text{Be}$ reaction rate has been evaluated and the corresponding coefficients reported in the right column of Table 1. Also, in this case, small variations ($\sim \pm 2\%$) have been found when comparing the obtained reaction rate with its parametrization of Equation (6) at temperatures of $T_9 < 0.2$. Figure 7 reports the ratio (blue line) between the THM and NACRE reaction rate, together with the corresponding uncertainties given by the available data, while Figure 8 reports the comparison between the THM and the NACREII reaction rate. A careful examination of both figures suggests a reduction of uncertainties at lower temperatures, i.e., close to the Gamow peak typical of quiescent boron burning, while at higher temperatures the THM reaction

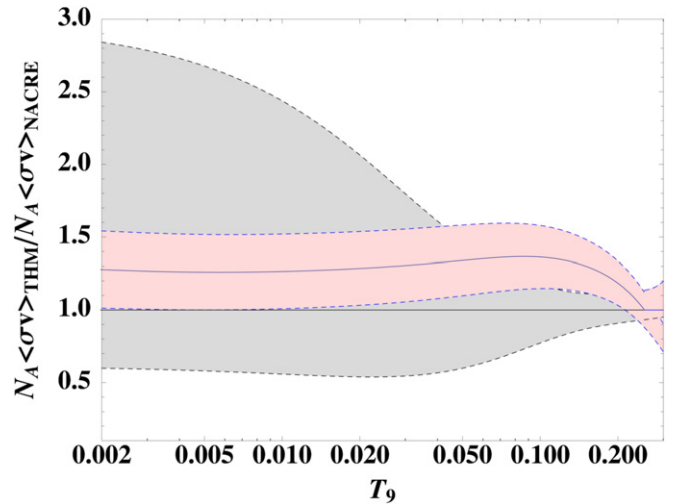


Figure 5. Ratio between the ${}^9\text{Be}(p,\alpha){}^6\text{Li}$ THM reaction rate and that given in the NACRE compilation. The THM reaction rate, valid for $T_9 < 0.2$, has been deduced by means of the $S(E)$ -factor given in Equation (4).

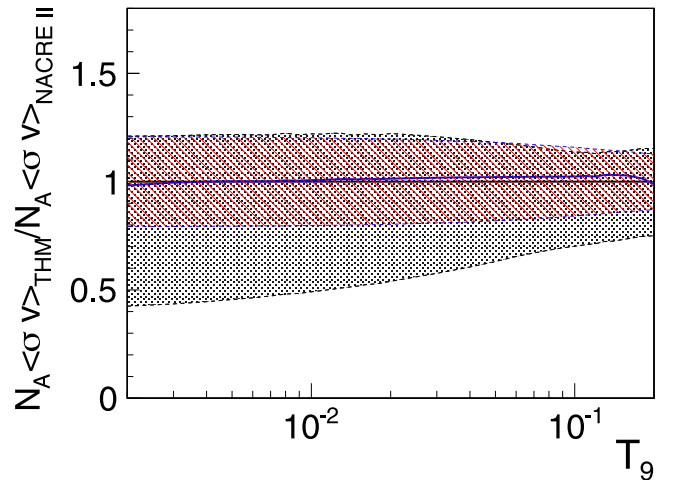


Figure 6. Ratio between the ${}^9\text{Be}(p,\alpha){}^6\text{Li}$ THM reaction rate extracted here and that listed in the NACREII compilation. Even if the ratio between the adopted values (red line) does not introduce any significant variation, the THM uncertainty region (blue dashed area) is clearly lowered with respect to the NACREII one (black dashed area).

rate is inevitably affected by the experimental uncertainties discussed in Spitaleri et al. (2014). However, besides the small deviations among the adopted values, the NACREII compilation reports the value of $S(0.001) = 1.3^{+0.2}_{-0.9} \times 10^3$ MeV b, while the THM data of Spitaleri et al. (2014) suggest $S(0.001) = 1405 \pm 450$ MeV b.

5. IMPLICATIONS FOR STELLAR PHYSICS

The described change in the ${}^9\text{Be}$ and ${}^{10}\text{B}$ proton burning rates due to the THM cross-section measurements is significant; thus it is worthwhile to evaluate their effects on stellar evolutionary models. The ${}^9\text{Be}$ and ${}^{10}\text{B}$ burning reactions are negligible regarding the stellar energetics, thus their effects on stellar structures are unimportant; however, a change in the burning rates sensibly affects Be and B surface abundances.

For the reasons discussed in the Introduction, we restrict our analysis on low-mass pre-MS stars; ${}^9\text{Be}$ and ${}^{10}\text{B}$ surface abundances obtained with the present rates are compared with

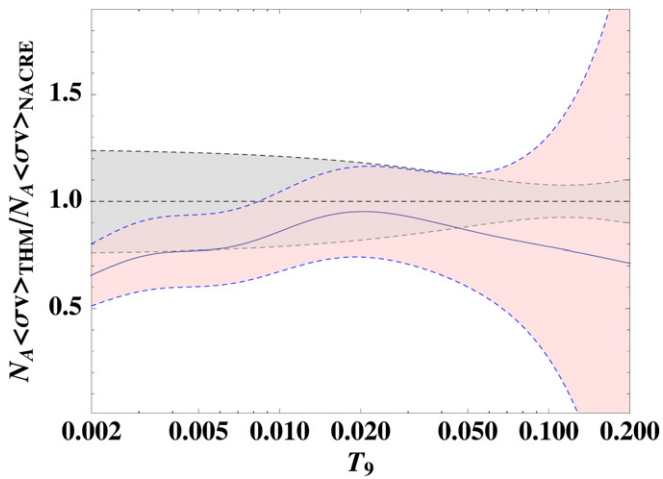


Figure 7. Ratio between the $^{10}\text{B}(p,\alpha)^7\text{Be}$ THM reaction rate and that given in the NACRE compilation (blue line). The red filled area marks the THM reaction rate uncertainties compared with the NACRE ones (gray area). At temperatures of a few millions of kelvin, the THM reaction rate is lowered by $\sim 30\%$.

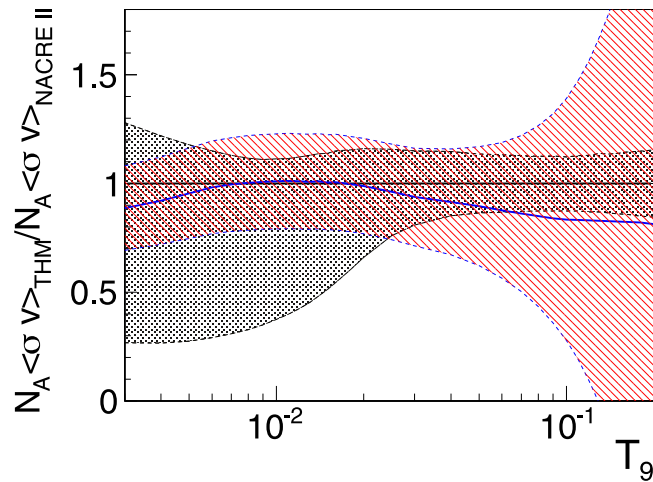


Figure 8. Ratio between the $^{10}\text{B}(p,\alpha)^7\text{Be}$ THM reaction rate and that given in the NACRE II compilation.

the ones resulting from the adoption of the still widely used NACRE compilation.

5.1. Stellar Evolution Models

Stellar evolutionary tracks are calculated by means of the PROSECCO stellar code derived from the well tested FRANEC one (see, e.g., Degl’Innocenti et al. 2008; Dell’Omodarme et al. 2012).⁶ The same input physics discussed in previous papers (Tognelli et al. 2011, 2012, 2015a, 2015b) have been adopted. Our code follows in detail all of the elements involved in nuclear burnings from the hydrogen up to the carbon burning. In particular, for the present work the temporal evolution of light elements, i.e., ^2H , $^6,^7\text{Li}$, ^9Be , and $^{10,11}\text{B}$, is followed in detail. The light element proton capture reaction rates are the same adopted in Tognelli et al. (2015b) with the exception of the THM reaction rates for the $^9\text{Be}(p,\alpha)^6\text{Li}$ and $^{10}\text{B}(p,\alpha)^7\text{Be}$, calculated in the present work. For these reactions,

⁶ Comparisons among our models and other evolutionary tracks largely used in the literature and/or observational data show a very good agreement, as discussed in Tognelli et al. (2011) and Dell’Omodarme et al. (2012).

the rates from the NACRE (Angulo et al. 1999) compilation have also been adopted for comparison. Bare nuclei reactions have been corrected to account for the plasma electron screening for weak (Salpeter 1954), weak-intermediate-strong (Dewitt et al. 1973; Graboske et al. 1973), and strong (Itoh et al. 1977, 1979) screening.

To cover the suitable range of stellar masses in which ^9Be and ^{10}B can be destroyed during the pre-MS phase, we computed models with masses between $0.06 M_{\odot}$ and $0.80 M_{\odot}$ (with a spacing of $\Delta M = 0.02 M_{\odot}$ for $M \leq 0.5 M_{\odot}$ and $\Delta M = 0.05 M_{\odot}$ for $M > 0.5 M_{\odot}$). Models have been evolved from the beginning of the Hayashi track (i.e., fully convective cold-objects with large radius and luminosity) up to the beginning of the MS phase.

To evaluate the effect of updating the ^9Be and ^{10}B burning reaction rates for the different stellar populations in our Galaxy, we adopted two chemical compositions: $[\text{Fe}/\text{H}] = +0.0$, for solar-like chemical composition stars, and $[\text{Fe}/\text{H}] = -1.5$ for metal-poor halo stars.⁷ $[\text{Fe}/\text{H}]$ has been converted into initial helium Y and metal Z mass fractional abundances by adopting Equations (1) and (2) in Gennaro et al. (2010); thus, the adopted $[\text{Fe}/\text{H}]$ values correspond to $(Y, Z) = (0.274, 0.0130)$ and $(Y, Z) = (0.249, 0.0004)$, respectively.

The initial ^9Be and ^{10}B abundances have been chosen according to the adopted $[\text{Fe}/\text{H}]$ value.⁸ For solar chemical composition, we used the following initial abundances⁹: $A(^9\text{Be}) = 1.32$ (Lodders 2010) and $N(^{10}\text{B}) = N(^{11}\text{B})/4.0$ (Prantzos 2012), where the initial ^{11}B abundance is fixed to $A(^{11}\text{B}) = 2.79$ (Cunha 2010). For metal-poor models, we adopted $A(^9\text{Be}) = 0.0$ (Boesgaard & Krugler Hollek 2009), $A(^{11}\text{B}) = 1.5$ (Cunha 2010), and $N(^{10}\text{B}) = N(^{11}\text{B})/4.5$ (Prantzos 2012).

Notice that all the calculations presented in this paper are performed in a differential way, i.e., the results obtained with the THM and the NACRE ^9Be and ^{10}B reaction rates are compared keeping all of the other physical parameters and the stellar chemical composition fixed. Additionally, the results are expected to be weakly dependent on the chemical composition, on the initial Be and B abundances, and on the input physics adopted in the models (see Valle et al. 2013a, 2013b).

5.2. ^9Be and ^{10}B Surface Abundances

As discussed in the Introduction, due to their low burning temperatures, ^9Be and ^{10}B are completely destroyed in hot stellar interiors, while their surface abundance depends on the temperature reached at the bottom of the external convective envelope. In order to understand the pre-MS surface abundance behavior, one has to remember that during this phase, the gravitational contraction leads to an increase of the stellar temperature until, at the pre-MS end, nuclear reactions provide the energy necessary to counterbalance the radiative losses at the stellar surface, stabilizing the structure on nuclear timescales.

⁷ By definition $[\text{Fe}/\text{H}] = \log(N_{\text{Fe}}/N_{\text{H}})_{*}/(N_{\text{Fe}}/N_{\text{H}})_{\odot}$, where N represents the numerical abundance.

⁸ Li, Be, and B abundances increase with metallicity, because the observed production is mainly the result of cosmic ray spallation processes (see, e.g., Prantzos 2012).

⁹ The abundances of light elements are usually given in terms of the numerical logarithmic abundance A , which is defined as $A = 12 + \log N/N(\text{H})$, where N and $N(\text{H})$ are, respectively, the considered element and the hydrogen numerical abundance.

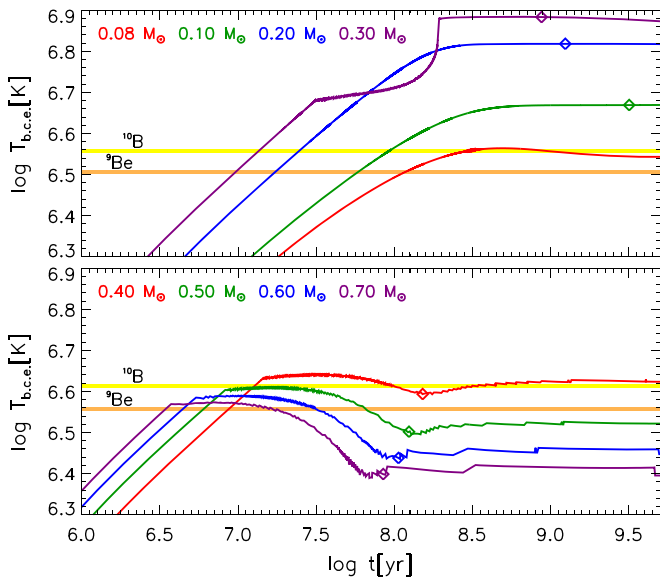


Figure 9. Temporal evolution of the temperature at the bottom of the convective envelope (or central temperature in fully convective stars), for stellar models with $M \in [0.08, 0.3] M_{\odot}$ (upper panel) and $M \in [0.4, 0.7] M_{\odot}$ (lower panel), with $[\text{Fe}/\text{H}] = +0.0$. The thick colored lines represent the temperature at which the burning of ${}^9\text{Be}$ (orange) and ${}^{10}\text{B}$ (yellow) becomes efficient for the selected mass range (see the text). Open diamonds approximately mark the beginning of the MS evolution.

At the first pre-MS stages stars are fully convective and the surface matter is continuously mixed with the stellar interior one. When the central temperature is high enough, the light elements start to be destroyed, thus changing their surface abundances because of the action of convective phenomena. However, as the central temperature increases, depending on the stellar mass, a radiative core develops while the envelope remains convective. Adopting a solar-like chemical composition (i.e., $[\text{Fe}/\text{H}] = +0.0$), for stellar masses lower than about $0.3 M_{\odot}$, such a radiative core never forms (or it only temporarily appears, as in the $0.3 M_{\odot}$ model) while, for higher masses, the larger the mass is, the lower the age is at which it is formed. If a radiative core is present, the surface matter can no longer reach the hottest central regions of the star, though it can be dragged down to a depth given by the extension of the convective envelope. Thus, the external matter experiences the maximum temperature (as well as the highest light element burning efficiency) at the bottom of the convective envelope, whose depth depends on both the stellar mass, age, and chemical composition. From this general discussion it emerges that the phase of efficient light element burning is strictly correlated with the formation of a radiative core in the star and on its temporal evolution.

Figure 9 shows the temporal evolution of the temperature at the bottom of the convective envelope ($T_{\text{b.c.e.}}$) for different masses, for stellar evolutionary models with $[\text{Fe}/\text{H}] = +0.0$, from the early pre-MS evolution up to the beginning of the MS (marked by an open diamond). The minimum mass plotted in the figure (i.e., $0.08 M_{\odot}$) approximately corresponds to the minimum mass (M_{min}) that reaches a central temperature high enough to burn ${}^9\text{Be}$ ($M_{\text{min}} \approx 0.07 M_{\odot}$) and ${}^{10}\text{B}$ ($M_{\text{min}} \approx 0.08 M_{\odot}$). For the selected chemical composition, masses larger than about $0.7 M_{\odot}$ do not deplete ${}^9\text{Be}$ (and consequently they do not destroy ${}^{10}\text{B}$) during the pre-MS and thus they are not shown. In Figure 9, we also plotted a rough mean temperature estimate at which

the ${}^9\text{Be}$ and ${}^{10}\text{B}$ begin to be destroyed, useful to make clearer the following discussion. Notice that ${}^9\text{Be}$ and ${}^{10}\text{B}$ ignition temperatures are different in the upper ($T({}^9\text{Be}) \approx 3.2 \times 10^6 \text{ K}$ and $T({}^{10}\text{B}) \approx 3.6 \times 10^6 \text{ K}$) and lower ($T({}^9\text{Be}) \approx 3.6 \times 10^6 \text{ K}$ and $T({}^{10}\text{B}) \approx 4.1 \times 10^6 \text{ K}$) panel. This happens because the rate at which an element is destroyed in stars depends not only on the temperature but also (even if weakly) on the density, which increases as the mass decreases, with a resulting decrease of the burning temperature.

Referring to the upper panel of Figure 9, models with $M < 0.3 M_{\odot}$ remain fully convective in pre-MS and MS. In these cases, $T_{\text{b.c.e.}}$ always corresponds to the central temperature which progressively increases as the star approaches the MS, where its maximum value is reached. Thus, the light element burning gets more and more efficient as the star evolves. The $M = 0.3 M_{\odot}$ is, approximately, the transition mass between stars that are always fully convective during the pre-MS and MS, and masses that develop a radiative core that continuously grows (in mass) in the pre-MS. In the $0.3 M_{\odot}$ model, a temporarily radiative core develops in the pre-MS, but it disappears before the star reaches its ZAMS location.¹⁰ Notice that the $T_{\text{b.c.e.}}$ of the $0.3 M_{\odot}$ model continues to increase even when the radiative core forms, but at a much reduced rate.

The models in the bottom panel of Figure 9 (i.e., $M \geq 0.4 M_{\odot}$) form a radiative core during the pre-MS, evidenced by the first plateau in $\log T_{\text{b.c.e.}}$. Even in these cases, during the first total convective phase $T_{\text{b.c.e.}}$, which coincides with the central temperature, increases following the stellar contraction. However, when the radiative core develops, it pushes the bottom of the convective envelope toward more and more external regions. In a first phase, the decrease of $T_{\text{b.c.e.}}$ caused by the growth (in mass) of the radiative core is counterbalanced by the temperature increase due to the stellar contraction and $T_{\text{b.c.e.}}$ almost stabilizes. However, as the star evolves toward the zero-age main sequence (ZAMS), the contraction rate slows down and $T_{\text{b.c.e.}}$ decreases, reaching its minimum value in ZAMS. Note that increasing the stellar mass the radiative core develops at early ages and reaches more external regions, thus lowering the maximum $T_{\text{b.c.e.}}$ value reached during the pre-MS evolution (and also $T_{\text{b.c.e.}}$ in ZAMS) and reducing the light element burning efficiency. For example, while for $M = 0.4 M_{\odot}$ in ZAMS the convective envelope contains about 40% of the stellar mass for $M = 0.7 M_{\odot}$ it reduces to about 10%.

From Figure 9, it is evident that, depending on the mass, the formation of a radiative core, pushing the convective envelope toward more external regions, might lead to a temperature at the bottom of the convective envelope that is lower than that needed to (efficiently) destroy the considered element. Regarding the masses for which this happens, the larger the mass is, the more rapid the shift of the convective envelope toward the surface is, and the earlier the temperature at the bottom of the convective envelope decreases below the burning threshold. Referring to Figure 9, one can see that while for $M \leq 0.4 M_{\odot}$, ${}^9\text{Be}$ is destroyed both in the pre-MS and in the MS, for masses between 0.5 and $0.7 M_{\odot}$ ${}^9\text{Be}$ is destroyed only in the pre-MS. Moreover, the temporal duration of the burning phase steeply decreases as the mass increases. For ${}^{10}\text{B}$, the transition mass is much sharper; indeed, while for $M \lesssim 0.4 M_{\odot}$, ${}^{10}\text{B}$ is destroyed both in the pre-MS and the MS, for $M > 0.5$, it is never destroyed.

¹⁰ The zero-age main sequence (ZAMS) corresponds to the beginning of the MS evolution.

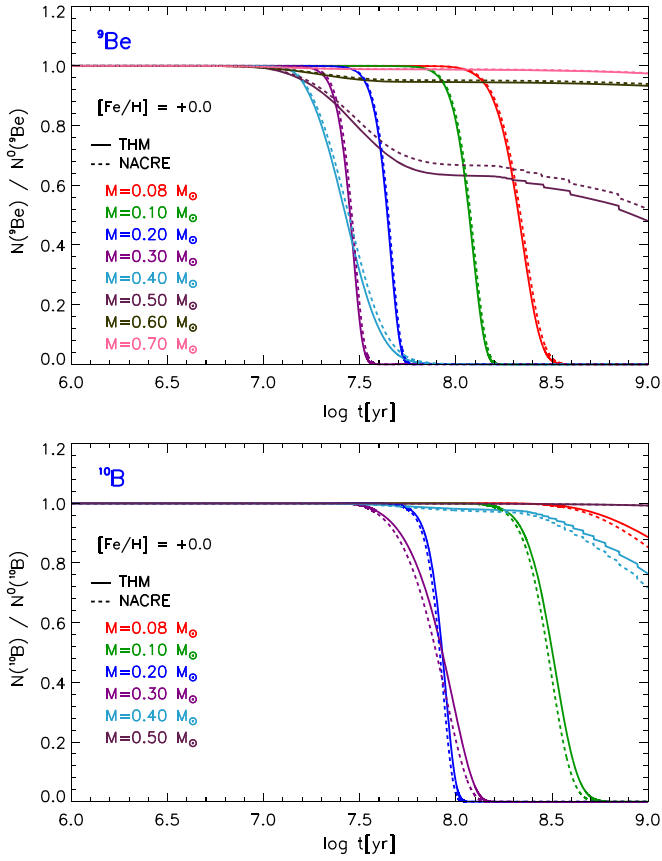


Figure 10. Temporal evolution of surface ${}^9\text{Be}$ (upper panel) and ${}^{10}\text{B}$ (lower panel) abundances (normalized to one) for models with the labelled stellar mass and $[\text{Fe}/\text{H}] = +0.0$. Models computed using the present THM (thick solid line) and the NACRE (dashed line) reaction rates are shown.

Figure 10 shows the temporal evolution of surface ${}^9\text{Be}$ (top panel) and ${}^{10}\text{B}$ abundance (bottom panel), normalized to one. The models have been computed adopting both the THM (solid line) and the NACRE (dashed line) reaction rates for the ${}^9\text{Be}(p,\alpha){}^6\text{Li}$ and ${}^{10}\text{B}(p,\alpha){}^7\text{Be}$ reactions. As discussed in Section 4, the THM rate for ${}^9\text{Be}$ burning is about 25% larger than the NACRE one (at the temperature of interest, see Figure 5), thus leading to a faster ${}^9\text{Be}$ destruction in the THM models. In addition, the adoption of a larger reaction rate at a given temperature reduces the age at which ${}^9\text{Be}$ depletion becomes efficient. Thus, at the same age, models with the THM rate show a lower ${}^9\text{Be}$ surface abundance with respect to models with the NACRE one.

The differences in the predicted surface abundances between the THM and NACRE models are significant if surface ${}^9\text{Be}$ is efficiently destroyed (i.e., for $M \lesssim 0.5 M_{\odot}$), while at larger masses they are quite negligible. The effect of the update of the ${}^9\text{Be}$ burning rate is also significant for $M \leq 0.3 M_{\odot}$ even if not clearly visible in the figure because of the steep decrease in the surface abundance (almost vertical in the plot).

It is worth noticing that in stellar models ${}^9\text{Be}$ is destroyed following two channels: (1) ${}^9\text{Be}(p,\alpha){}^6\text{Li}$ (R_1 , the rate analyzed here) and (2) ${}^9\text{Be}(p, 2\alpha){}^2\text{H}$ (R_2). The ratio between the ${}^9\text{Be}(p,\alpha){}^6\text{Li}$ and ${}^9\text{Be}(p, 2\alpha){}^2\text{H}$ reaction rates in stellar conditions at the temperature of interest is $R_1/R_2 \approx 1.2$, thus the ${}^9\text{Be}(p, 2\alpha){}^2\text{H}$ contribution to beryllium destruction is not negligible. As a consequence, the reaction rate variation for the first channel affects the final beryllium abundance for a factor

that is given by the reaction rate change (about 25%) multiplied by the probability that the ${}^9\text{Be}$ burning occurs in that channel, i.e., $25\% \times R_1/(R_1 + R_2) \approx 14\%$.

The predicted temporal evolution of the ${}^{10}\text{B}$ surface abundance for the selected stellar masses is shown in the bottom panel of Figure 10. In this case the THM ${}^{10}\text{B}$ burning rate is smaller (by about 25%), at the temperatures of interest, with respect to the NACRE one, thus leading to a less pronounced ${}^{10}\text{B}$ destruction in the THM models and to a larger surface ${}^{10}\text{B}$ abundance at a fixed age. Because of the larger ${}^{10}\text{B}$ burning temperature with respect to the ${}^9\text{Be}$ one, the effect of changing the reaction rate is relevant only for masses $M \lesssim 0.4 M_{\odot}$. Also notice that the typical timescale at fixed mass in which ${}^{10}\text{B}$ is destroyed is longer than that corresponding to ${}^9\text{Be}$.

We mention that for ages typical of the MS evolution, microscopic diffusion might become a dominant effect in determining the surface abundance of light elements. As an example, such an effect is visible in Figure 10, for $\log t \gtrsim 8.5$, in the case of $M = 0.5 M_{\odot}$ for ${}^9\text{Be}$ and of $M = 0.4 M_{\odot}$ for ${}^{10}\text{B}$. However, the efficiency of diffusion is independent of the analyzed burning reaction rates, and being only interested in the pure effect of nuclear burnings, we only mention it without further discussions.

The panels of Figure 10 are useful for understanding the impact of the updated reaction rates on the theoretical expectations. Additionally, for an easier comparison between the theoretical predictions made here and the observational data, we have also reported the predicted ${}^9\text{Be}$ and ${}^{10}\text{B}$ abundances for several stellar masses as a function of the effective temperature, T_{eff} , thus defining the $A(X)$ versus the T_{eff} plane. Since this plot is often used when studying galactic open clusters for which the comparison between observations and models is made at a fixed age (i.e., that of the cluster), three different ages, suitable for ${}^9\text{Be}$ and ${}^{10}\text{B}$ depletion timescales, have been selected in the figure, namely 50, 100, and 300 Myr for ${}^9\text{Be}$ depletion and 100, 200, and 500 Myr for the analysis of ${}^{10}\text{B}$.

The panels in Figure 11 show, for each selected age, the comparison between the surface logarithmic abundances obtained using the THM and NACRE reaction rates as a function of the effective temperature, for $[\text{Fe}/\text{H}] = +0.0$. Each curve represents the abundance isochrone, i.e., the locus of models with the same age but different masses, in the range $[0.06, 0.8] M_{\odot}$. The surface abundances are shown as a function of T_{eff} , which does not change with the variation of ${}^9\text{Be}$ and ${}^{10}\text{B}$ reaction rates. To clearly show the impact of the new reaction rates on the surface abundances, Table 2 lists the effective temperature, the corresponding mass, and the surface depletion levels, namely,

$$\Delta A({}^9\text{Be}) \equiv A({}^9\text{Be}) - A_{\text{ini}}({}^9\text{Be}) \equiv \log \frac{N({}^9\text{Be})}{N_{\text{ini}}({}^9\text{Be})}$$

$$\Delta A({}^{10}\text{B}) \equiv A({}^{10}\text{B}) - A_{\text{ini}}({}^{10}\text{B}) \equiv \log \frac{N({}^{10}\text{B})}{N_{\text{ini}}({}^{10}\text{B})}.$$

These have been evaluated for some of the models plotted in Figure 11 by means of both THM and NACRE reaction rates.

As expected, the models that do not efficiently destroy ${}^9\text{Be}$ (${}^{10}\text{B}$) are not affected by the reaction rate variation. The situation is different moving toward the region where ${}^9\text{Be}$ (${}^{10}\text{B}$)

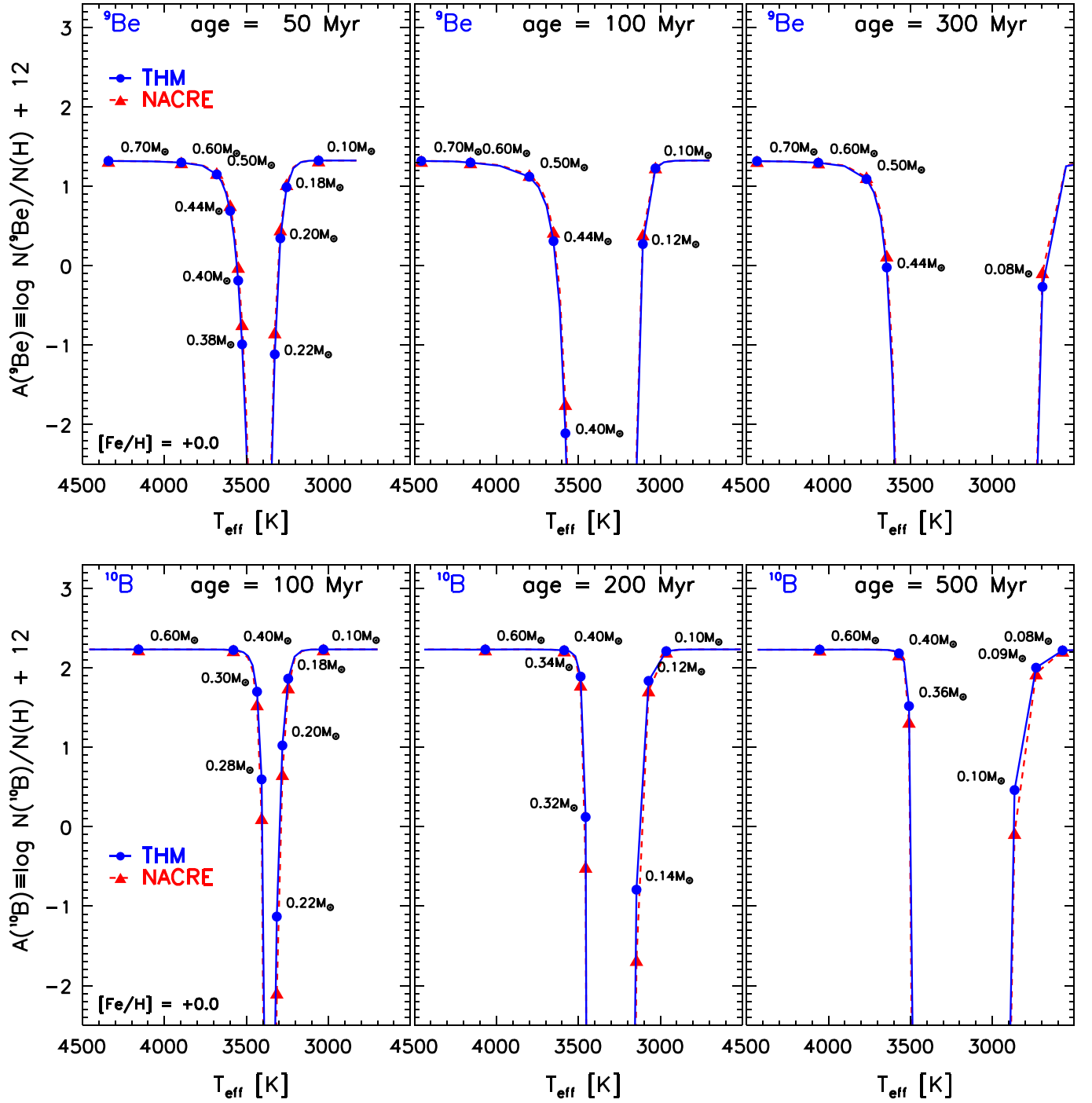


Figure 11. Surface logarithmic abundances of ${}^9\text{Be}$ (upper panel) and ${}^{10}\text{B}$ (lower panel) as a function of the star effective temperature for three labelled ages. Models are computed for $[\text{Fe}/\text{H}] = +0.0$ in the mass range of $[0.06, 0.8] M_{\odot}$, adopting both the present THM (solid blue line) and the NACRE (dashed red line) reaction rates. Filled circles and triangles mark the position of some specific stellar models computed using, respectively, the THM and NACRE reaction rates.

is destroyed ($T_{\text{eff}} \lesssim 3600$ K); in this case, the differences between the adoption of the NACRE and THM reaction rates can be as large as about -1 dex for ${}^9\text{Be}$ and almost 2 dex for ${}^{10}\text{B}$.

Notice that the temperature range where the efficient depletion occurs depends on both the age and the considered element. For a 50 Myr age, the ${}^9\text{Be}$ depletion occurs for $3300 \text{ K} \lesssim T_{\text{eff}} \lesssim 3700 \text{ K}$, while for larger ages the range shifts to $[3000, 3800] \text{ K}$ at 100 Myr and to $[2600, 3800] \text{ K}$ at 500 Myr. The ${}^{10}\text{B}$ shows, at a fixed age, a thinner range of effective temperature for which burning is efficient, about

$[3200, 3500] \text{ K}$ for 100 Myr, $[3000, 3500] \text{ K}$ at 200 Myr, and $[2800, 3500] \text{ K}$ for ages of 500 Myr.

As anticipated in Section 5.1, stellar models with $[\text{Fe}/\text{H}] = -1.5$ have also been computed and the corresponding results reported in Figure 12. The corresponding T_{eff} , stellar mass values and surface depletion levels, namely $\Delta A({}^9\text{Be})$ and $\Delta A({}^{10}\text{B})$, for some of the models plotted in Figure 12 are listed in Table 3, similarly to the $[\text{Fe}/\text{H}] = +0.0$ case of Table 2.

As is well known, by changing the chemical composition, the degree of depletion at a given age and mass changes. This is

Table 2
Temperature, Mass, and Depletion Levels of ${}^9\text{Be}$ and ${}^{10}\text{B}$ Surface Logarithm Abundances for Some of the Models Plotted in Figure 11,
Computed with the THM and NACRE Reaction Rates, for $[\text{Fe}/\text{H}] = +0.0$

Element: ${}^9\text{Be}$, $A_{\text{ini}}({}^9\text{Be}) = 1.32$, $[\text{Fe}/\text{H}] = +0.0$											
50 Myr				100 Myr				300 Myr			
$T_{\text{eff}}(\text{K})$	M/M_{\odot}	ΔA THM	ΔA NACRE	$T_{\text{eff}}(\text{K})$	M/M_{\odot}	ΔA_{THM}	ΔA_{NACRE}	$T_{\text{eff}}(\text{K})$	M/M_{\odot}	ΔA_{THM}	ΔA_{NACRE}
3059	0.10	-0.00	-0.00	2912	0.08	-0.00	-0.00	2695	0.08	-1.55	-1.37
3168	0.14	-0.02	-0.02	3030	0.10	-0.09	-0.08	2914	0.10	<-10.00	<-10.00
3255	0.18	-0.32	-0.28	3161	0.14	-5.07	-4.77	3609	0.42	-2.76	-2.46
3326	0.22	-2.35	-2.09	3244	0.18	<-10.00	<-10.00	3681	0.46	-0.71	-0.63
3384	0.26	-9.36	-8.28	3547	0.38	-5.74	-5.39	3767	0.50	-0.23	-0.20
3433	0.30	-9.29	-8.07	3613	0.42	-1.85	-1.63	4062	0.60	-0.03	-0.02
3480	0.34	-4.86	-4.47	3694	0.46	-0.57	-0.50
3526	0.38	-2.30	-2.04	3798	0.50	-0.20	-0.18
3574	0.42	-0.97	-0.86	4160	0.60	-0.02	-0.02
3624	0.46	-0.40	-0.36
3680	0.50	-0.17	-0.15
3893	0.60	-0.02	-0.02

Element: ${}^{10}\text{B}$, $A_{\text{ini}}({}^{10}\text{B}) = 2.20$, $[\text{Fe}/\text{H}] = +0.0$											
100 Myr				200 Myr				500 Myr			
$T_{\text{eff}}(\text{K})$	M/M_{\odot}	ΔA THM	ΔA NACRE	$T_{\text{eff}}(\text{K})$	M/M_{\odot}	ΔA_{THM}	ΔA_{NACRE}	$T_{\text{eff}}(\text{K})$	M/M_{\odot}	ΔA_{THM}	ΔA_{NACRE}
3161	0.14	-0.02	-0.02	2964	0.10	-0.02	-0.03	2864	0.10	-1.76	-2.30
3244	0.18	-0.36	-0.47	3145	0.14	-3.00	-3.89	3131	0.14	<-10.00	<-10.00
3314	0.22	-3.32	-4.26	3239	0.18	<-10.00	<-10.00	3480	0.34	-6.01	-7.74
3377	0.26	-7.26	-9.46	3486	0.34	-0.34	-0.44	3538	0.38	-0.16	-0.19
3434	0.30	-0.53	-0.69	3551	0.38	-0.03	-0.03	3603	0.42	-0.02	-0.02
3489	0.34	-0.08	-0.11	3622	0.42	-0.00	-0.01
3547	0.38	-0.02	-0.02
3613	0.42	-0.00	-0.01
3694	0.46	-0.00	-0.00
3798	0.50	-0.00	-0.00
4160	0.60	-0.00	-0.00

Note. The adopted initial ${}^9\text{Be}$ and ${}^{10}\text{B}$ logarithm abundance A_{ini} is indicated in each table.

expected because the adopted chemical composition affects the structure of a star, thus its effective temperature (a reduction of the metallicity produces hotter models), convective envelope extension, age, etc.

The comparison between the models in Figures 11 and 12 evidences the shift and the lengthening of the effective temperature range where ${}^9\text{Be}$ or ${}^{10}\text{B}$ are efficiently destroyed. Furthermore, one can see that the effect of the updated reaction rates in the $A(X)$ versus the T_{eff} plane at a given age and fixed depletion level from the original ${}^9\text{Be}$, ${}^{10}\text{B}$ values is similar when calculating $[\text{Fe}/\text{H}] = -1.5$ or $[\text{Fe}/\text{H}] = +0.0$ models. This is even clearer if one compares, in Tables 2 and 3, the differences between columns ΔA_{THM} and ΔA_{NACRE} (taken at approximately the same level of surface depletion, ΔA_{THM}) for the two $[\text{Fe}/\text{H}]$ values. As an example, for a surface ${}^9\text{Be}$ reduction of about 1 dex (i.e., $A({}^9\text{Be}) \approx 0$ for $[\text{Fe}/\text{H}] = +0.0$ and $A({}^9\text{Be}) \approx -1$ for $[\text{Fe}/\text{H}] = -1.5$) the adoption of the THM instead of the NACRE reaction rate leads to a reduction of the surface logarithmic abundance of 0.1–0.2 dex in both $[\text{Fe}/\text{H}] = +0.0$ and $[\text{Fe}/\text{H}] = -1.5$ models. This clearly indicates that the effect of the change of the ${}^9\text{Be}$ and ${}^{10}\text{B}$ reaction rates on the predicted depletion level is weakly dependent on the adopted metallicity.

Another point worth discussing is the effect of the ${}^{10}\text{B}$ reaction rate on the $N({}^{11}\text{B})/N({}^{10}\text{B})$ ratio. Figure 13 shows the temporal evolution of the ${}^{11}\text{B}$ – ${}^{10}\text{B}$ numerical abundance ratio for several masses, for $[\text{Fe}/\text{H}] = +0.0$ (top panel) and $[\text{Fe}/\text{H}] = -1.5$ (bottom panel). Models have been computed by using the THM (full line) and the NACRE (dashed line) ${}^{10}\text{B}(p,\alpha){}^7\text{Be}$ reaction rate. The points corresponding to a surface ${}^{10}\text{B}$ reduction of 80%, 50%, 10%, and 1%, with respect to its initial abundance, are also marked in the plot.

The initial $N({}^{11}\text{B})/N({}^{10}\text{B})$ is 4 for $[\text{Fe}/\text{H}] = +0.0$ and 4.5 for $[\text{Fe}/\text{H}] = -1.5$ models (as discussed in Section 5.1), but it significantly changes in time in those models that destroy boron (i.e., $0.1 \lesssim M/M_{\odot} \lesssim 0.3$). This is expected, because the depletion of ${}^{10}\text{B}$ and ${}^{11}\text{B}$ occurs at different ages, due to the slightly different “ignition” temperatures (about 4×10^6 K for ${}^{10}\text{B}$ and 5×10^6 K for ${}^{11}\text{B}$), the ${}^{10}\text{B}$ burning starting at younger ages. Consequently, the $N({}^{11}\text{B})/N({}^{10}\text{B})$ value is expected to increase with time.

As already discussed, the new ${}^{10}\text{B}$ THM reaction rate is smaller, at a given temperature, than the NACRE one. This produces a shift of the ${}^{10}\text{B}$ depletion at progressively larger ages. This feature is clearly visible in Figure 13; the change of the ${}^{10}\text{B}$ reaction rate has a strong impact on the $N({}^{11}\text{B})/N({}^{10}\text{B})$ ratio at a fixed age, and the differences increase with the

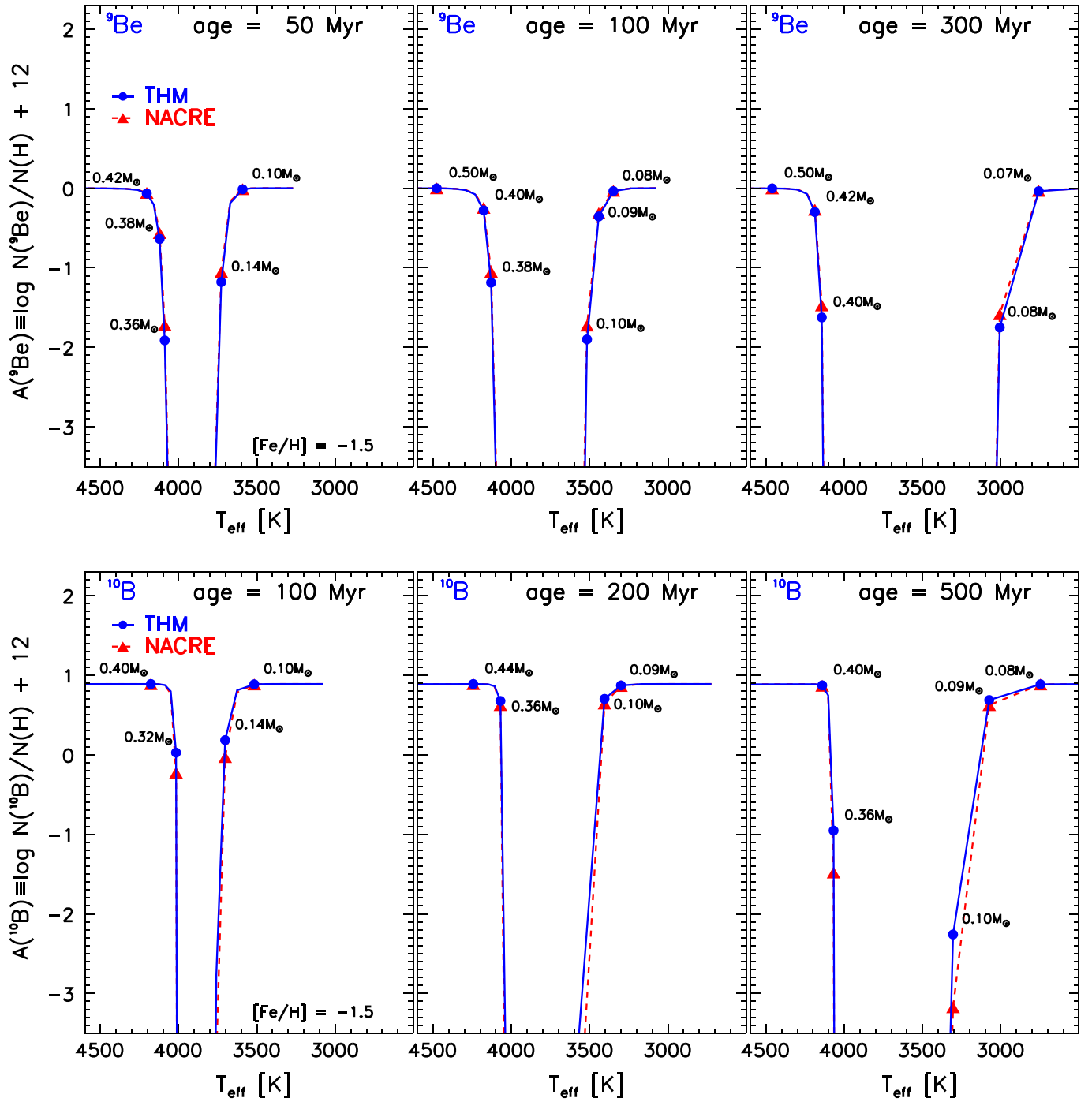


Figure 12. Same as in Figure 11 but for models with $[\text{Fe}/\text{H}] = -1.5$.

depletion degree. Notice that the effect on the predicted $N({}^{11}\text{B})/N({}^{10}\text{B})$ value of updating the ${}^{10}\text{B}$ reaction rate is weakly affected by the adopted metallicity, as already discussed.

6. CONCLUSIONS

The light elements lithium, beryllium, and boron offer an important opportunity for a deeper understanding of stellar structures and mixing phenomena. They are destroyed by nuclear reactions at temperatures of a few millions of kelvin and thus their surface abundances depend on the temperature reached at the bottom of the external convective envelope (that is on its depth) in which the matter is completely mixed.

For this reason spectroscopic observations of light element stellar surface abundances allow us to constrain the available theoretical models. By focusing our attention on pre-MS models, we evaluated the impact of the updated THM reaction rates for the two (p,α) destruction channels of the ${}^9\text{Be}$ and ${}^{10}\text{B}$ isotopes. A variation of the quoted rates is expected to affect light element external abundances only, leaving the stellar structure unchanged. THM allows the experimentalists to get low-energy $S(E)$ -factor measurements without the need for extrapolations, thus strongly reducing the uncertainties typical of direct determinations. In the present work, the THM ${}^9\text{Be}(p,\alpha){}^6\text{Li}$ $S(E)$ -factor measurement by Wen et al.

Table 3
The Same as in Table 2, but for the $[\text{Fe}/\text{H}] = -1.5$ Models Plotted in Figure 12

Element: ${}^9\text{Be}$, $A_{\text{ini}}({}^9\text{Be}) = 0.00$, $[\text{Fe}/\text{H}] = -1.5$											
50 Myr				100 Myr				300 Myr			
$T_{\text{eff}}(\text{K})$	M/M_{\odot}	ΔA_{THM}	ΔA_{NACRE}	$T_{\text{eff}}(\text{K})$	M/M_{\odot}	ΔA_{THM}	ΔA_{NACRE}	$T_{\text{eff}}(\text{K})$	M/M_{\odot}	ΔA_{THM}	ΔA_{NACRE}
3591	0.10	-0.01	-0.01	3348	0.08	-0.04	-0.03	3006	0.08	-1.75	-1.58
3727	0.14	-1.18	-1.05	3517	0.10	-1.90	-1.73	3348	0.10	<-10.00	<-10.00
3811	0.18	-9.30	-8.08	3703	0.14	<-10.00	<-10.00	4188	0.42	-0.30	-0.27
3880	0.22	<-10.00	<-10.00	4130	0.38	-1.19	-1.05	4300	0.46	-0.02	-0.02
4059	0.34	-4.52	-4.33	4233	0.42	-0.08	-0.07	4460	0.50	-0.00	-0.00
4122	0.38	-0.64	-0.56	4353	0.46	-0.01	-0.01
4204	0.42	-0.07	-0.06	4477	0.50	-0.00	-0.00
4335	0.46	-0.01	-0.01
4566	0.50	-0.00	-0.00
Element: ${}^{10}\text{B}$, $A_{\text{ini}}({}^{10}\text{B}) = 0.85$, $[\text{Fe}/\text{H}] = -1.5$											
100 Myr				200 Myr				500 Myr			
$T_{\text{eff}}(\text{K})$	M/M_{\odot}	ΔA_{THM}	ΔA_{NACRE}	$T_{\text{eff}}(\text{K})$	M/M_{\odot}	ΔA_{THM}	ΔA_{NACRE}	$T_{\text{eff}}(\text{K})$	M/M_{\odot}	ΔA_{THM}	ΔA_{NACRE}
3517	0.10	-0.00	-0.00	3169	0.08	-0.00	-0.00	2746	0.08	-0.00	-0.00
3703	0.14	-0.70	-0.92	3405	0.10	-0.19	-0.24	3304	0.10	-3.15	-4.06
3803	0.18	<-10.00	<-10.00	3673	0.14	<-10.89	<-10.89	3666	0.14	<-10.89	<-10.89
4051	0.34	-0.09	-0.12	4037	0.34	-4.63	-5.92	4102	0.38	-0.14	-0.18
4130	0.38	-0.00	-0.00	4107	0.38	-0.03	-0.04	4184	0.42	-0.00	-0.00
4233	0.42	-0.00	-0.00	4192	0.42	-0.00	-0.00

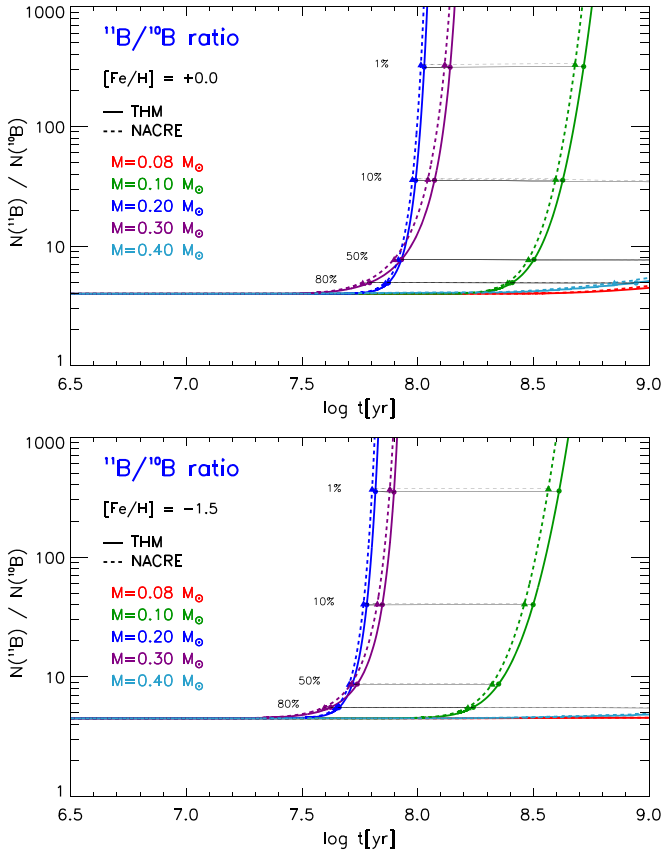


Figure 13. $N({}^{11}\text{B})/N({}^{10}\text{B})$ temporal evolution for stellar models with the labelled masses, for $[\text{Fe}/\text{H}] = +0.0$ (top panel) and $[\text{Fe}/\text{H}] = -1.5$ (bottom panel). The points where the surface ${}^{10}\text{B}$ abundance is reduced to 80%, 50%, 10%, and 1% of its initial value are marked.

(2008) and the ${}^{10}\text{Be}(p,\alpha){}^7\text{Be}$ $S(E)$ -factor evaluation by Spitaleri et al. (2014) have been used to calculate the corresponding reaction rates for which analytical forms have been given with the parameters shown in Table 1. The obtained rates have been compared with the NACRE ones, widely adopted in the astrophysical literature, finding, at temperatures of about $(3-5) \times 10^6$ K, variations of $\sim 25\%$ in both cases.

Then, we calculated stellar evolutionary models in the mass range of $[0.06, 0.8] M_{\odot}$ from the pre-MS to the MS phase by varying only the evaluated reaction rates from NACRE to THM. The temporal behavior of the surface ${}^9\text{Be}$ and ${}^{10}\text{B}$ abundances, for $[\text{Fe}/\text{H}] = +0.0$, when the NACRE and THM reaction rates are alternatively adopted is reported in Figure 10 showing, in some cases, significant variations. Moreover to reproduce typical observations in galactic open clusters, we also evaluated the ${}^9\text{Be}$ and ${}^{10}\text{B}$ abundances for different masses (effective temperatures) at fixed ages, for two metallicities typical of galactic and halo clusters, namely $[\text{Fe}/\text{H}] = +0.0$ and $[\text{Fe}/\text{H}] = -1.5$. The plots shown in Figures 11 and 12 clearly underline the differences in the results when the reaction rates change from NACRE to THM, especially for models for which an efficient ${}^9\text{Be}$ or ${}^{10}\text{B}$ burning is expected. An interesting example are models with masses of about $0.08 \lesssim M/M_{\odot} \lesssim 0.5$ in the temperature range of 2600–3600 K (for $[\text{Fe}/\text{H}] = +0.0$) or 3000–4000 K (for $[\text{Fe}/\text{H}] = -1.5$) for which a maximum difference of the ${}^9\text{Be}$ and ${}^{10}\text{B}$ logarithmic abundances of more than 1 dex, has been found. We emphasize that the effect of the reaction rate update is weakly dependent on the adopted metallicity, if the same level of depletion is considered. We also showed that the change of the ${}^{10}\text{B}$ reaction rate update has a significant impact in the predicted $N({}^{11}\text{B})/N({}^{10}\text{B})$ temporal evolution.

Although observational ^9Be and ^{10}B abundances are still not available for the low temperature/masse regimes typical of efficient ^9Be and/or ^{10}B burning (i.e., $T_{\text{eff}} \lesssim 4000\text{ K}$), the present work is an attempt to estimate the role of the improvements in nuclear physics in the computation of realistic and accurate theoretical stellar evolutionary models.

This work has been partially supported by the Italian Ministry of the University under grant RBF082838 and “LNS-Astrofisica Nucleare (fondi premiali)” by PRIN-MIUR 2010-2011 (*Chemical and dynamical evolution of the Milky Way and Local Group galaxies*, PI F. Matteucci), by PRIN-INAF 2012 (*The M4 Core Project with Hubble Space Telescope*, PI L. Bedin), and by INFN (*Iniziativa specifica TAsP*).

REFERENCES

- Angulo, C., Arnould, M., Rayet, M., et al. 1999, *NuPhA*, **656**, 3
- Angulo, C., Engstler, S., Raimann, G., et al. 1993, *ZPhyA*, **345**, 231
- Asplund, M., Grevesse, N., & Sauval, A. J. 2005, in ASP Conf. Ser. 336, *Cosmic Abundances as Records of Stellar Evolution and Nucleosynthesis*, ed. T. G. Barnes, III & F. N. Bash (San Francisco, CA: ASP), 25
- Asplund, M., Grevesse, N., Sauval, A. J., & Scott, P. 2009, *ARA&A*, **47**, 481
- Assenbaum, H. J., Langanke, K., & Rolfs, C. 1987, *ZPhyA*, **327**, 461
- Balachandran, S. C., & Bell, R. A. 1998, *Natur*, **392**, 791
- Baraffe, I., & Chabrier, G. 2010, *A&A*, **521**, A44
- Baur, G. 1986, *PhLB*, **178**, 135
- Boesgaard, A. M., Deliyannis, C. P., & Steinhauer, A. 2005, *ApJ*, **621**, 991
- Boesgaard, A. M., & Krugler Hollek, J. 2009, *ApJ*, **691**, 1412
- Burke, C. J., Pinsonneault, M. H., & Sills, A. 2004, *ApJ*, **604**, 272
- Burrows, A., Hubbard, W. B., Lumine, J. I., & Liebert, J. 2001, *RvMP*, **73**, 719
- Charbonnel, C., Deliyannis, C. P., & Pinsonneault, M. 2000, in IAU Symp. 198, *The Light Elements and their Evolution*, ed. L. da Silva, R. de Medeiros & M. Spite (San Francisco, CA: ASP), 87
- Chaussidon, M., & Robert, F. 1995, *Natur*, **374**, 337
- Cherubini, S., Kondratyev, V. N., Lattuada, M., et al. 1996, *ApJ*, **457**, 855
- Chmielewski, Y., Brault, J. W., & Mueller, E. A. 1975, *A&A*, **42**, 37
- Cunha, K. 2010, in IAU Symp. 268, *Light Elements in the Universe*, ed. C. Charbonnel et al. (Cambridge: Cambridge Univ. Press), 243
- D’Antona, F., & Montalbán, J. 2003, *A&A*, **412**, 213
- Degl’Innocenti, S., Prada Moroni, P. G., Marconi, M., & Ruoppo, A. 2008, *Ap&SS*, **316**, 25
- Delgado Mena, E., Israelian, G., González Hernández, J. I., Santos, N. C., & Rebolo, R. 2012, *ApJ*, **746**, 47
- Deliyannis, C. P., Pinsonneault, M. H., & Charbonnel, C. 2000, in IAU Symp. 198, *The Light Elements and their Evolution*, ed. L. da Silva, R. de Medeiros & M. Spite (San Francisco, CA: ASP), 61
- Dell’Omodarme, M., Valle, G., Degl’Innocenti, S., & Prada Moroni, P. G. 2012, *A&A*, **540**, A26
- Dewitt, H. E., Graboske, H. C., & Cooper, M. S. 1973, *ApJ*, **181**, 439
- Di Criscienzo, M., Ventura, P., & D’Antona, F. 2009, *A&A*, **496**, 223
- Dotter, A., Chaboyer, B., Jevremović, D., et al. 2008, *ApJS*, **178**, 89
- García Lopez, R. J., Rebolo, R., & Perez de Taoro, M. R. 1995, *A&A*, **302**, 184
- Gennaro, M., Prada Moroni, P. G., & Degl’Innocenti, S. 2010, *A&A*, **518**, A13
- Graboske, H. C., Dewitt, H. E., Grossman, A. S., & Cooper, M. S. 1973, *ApJ*, **181**, 457
- Grineviciute, J., Lamia, L., Mukhamedzhanov, A. M., Spitaleri, C., & La Cognata, M. 2015, *PhRvC*, **91**, 014601
- Gulino, M., Spitaleri, C., Cherubini, S., et al. 2010, *JPhG*, **37**, 125105
- Gulino, M., Spitaleri, C., Tang, X. D., et al. 2013, *PhRvC*, **87**, 012801
- Itoh, N., Totsuji, H., & Ichimaru, S. 1977, *ApJ*, **218**, 477
- Itoh, N., Totsuji, H., Ichimaru, S., & Dewitt, H. E. 1979, *ApJ*, **234**, 1079
- Jeffries, R. D. 2000, in ASP Conf. Ser. 198, *Stellar Clusters and Associations: Convection, Rotation, and Dynamos*, ed. R. Pallavicini, G. Micela & S. Sciortino (San Francisco, CA: ASP), 245
- Jeffries, R. D. 2006, in *ESO Astrophysics Symp.*, *Chemical Abundances and Mixing in Stars in the Milky Way and its Satellites*, ed. S. Randich & L. Pasquini (Berlin: Springer), 163
- Kaufer, A. 2010, in IAU Symp. 268, *Light Elements in the Universe*, ed. C. Charbonnel et al. (Cambridge: Cambridge Univ. Press), 317
- La Cognata, M., Mukhamedzhanov, A. M., Spitaleri, C., et al. 2011, *ApJL*, **739**, L54
- La Cognata, M., Spitaleri, C., Mukhamedzhanov, A., et al. 2010, *ApJ*, **708**, 796
- La Cognata, M., Spitaleri, C., Trippella, O., et al. 2012, *PhRvL*, **109**, 232701
- Lambert, D. L., Sheffer, Y., Federman, S. R., et al. 1998, *ApJ*, **494**, 614
- Lamia, L., La Cognata, M., Spitaleri, C., Irgaziev, B., & Pizzone, R. G. 2012a, *PhRvC*, **85**, 025805
- Lamia, L., Romano, S., Carlin, N., et al. 2007, *NuPhA*, **787**, 309
- Lamia, L., Spitaleri, C., Burjan, V., et al. 2012b, *JPhG*, **39**, 015106
- Lamia, L., Spitaleri, C., Carlin, N., et al. 2008, *NCimC*, **31**, 423
- Lamia, L., Spitaleri, C., La Cognata, M., Palmerini, S., & Pizzone, R. G. 2012c, *A&A*, **541**, A158
- Lamia, L., Spitaleri, C., Pizzone, R. G., et al. 2013, *ApJ*, **768**, 65
- Lodders, K. 2003, *ApJ*, **591**, 1220
- Lodders, K. 2010, in *Principles and Perspectives in Cosmochemistry*, ed. A. Goswami & B. E. Reddy (Berlin: Springer), 379
- Lodders, K., Plame, H., & Gail, H. 2009, in *Landolt-Börnstein—Group VI Astronomy and Astrophysics Numerical Data and Functional Relationships in Science and Technology*, Vol. 4B, ed. J. E. Trümper (Berlin: Springer), 44
- Montalbán, J., & D’Antona, F. 2006, *MNRAS*, **370**, 1823
- Montalbán, J., & Schatzman, E. 2000, *A&A*, **354**, 943
- Palmerini, S., Sergi, M. L., La Cognata, M., et al. 2013, *ApJ*, **764**, 128
- Piau, L., & Turck-Chièze, S. 2002, *ApJ*, **566**, 419
- Pinsonneault, M. H., Charbonnel, C., & Deliyannis, C. P. 2000, in IAU Symp. 198, *The Light Elements and their Evolution*, ed. L. da Silva, R. de Medeiros & M. Spite (San Francisco, CA: ASP), 74
- Pizzone, R. G., Spartá, R., Bertulani, C. A., et al. 2014, *ApJ*, **786**, 112
- Pizzone, R. G., Tumino, A., degl’Innocenti, S., et al. 2005, *A&A*, **438**, 779
- Prantzos, N. 2012, *A&A*, **542**, A67
- Proffitt, C. R., & Quigley, M. F. 1999, *BAAS*, **31**, 1448
- Randich, S., Primas, F., Pasquini, L., Sestito, P., & Pallavicini, R. 2007, *A&A*, **469**, 163
- Rebull, L., Duncan, D., Johansson, S., Thorburn, J., & Fields, B. 1998, *ApJ*, **507**, 387
- Rolfs, C. E., & Rodney, W. S. 1988, *Cauldrons in the Cosmos: Nuclear Astrophysics* (Chicago, IL: Univ. Chicago Press), 1988
- Romano, S., Lamia, L., Spitaleri, C., et al. 2006, *EPJA*, **27**, 221
- Salpeter, E. E. 1954, *AuJPh*, **7**, 373
- Santos, N. C., Israelian, G., Randich, S., García López, R. J., & Rebolo, R. 2004, *A&A*, **425**, 1013
- Sergi, M. L., Spitaleri, C., La Cognata, M., et al. 2010, *PhRvC*, **82**, 032801
- Shapiro, I. S. 1967, in *Interaction of High-Energy Particles with Nuclei*, ed. T. E. O. Ericson (New York: Academic Press), 210
- Sierk, A. J., & Tombrello, T. A. 1973, *NuPhA*, **210**, 341
- Simonucci, S., Taioli, S., Palmerini, S., & Busso, M. 2013, *ApJ*, **764**, 118
- Smiljanic, R., Randich, S., & Pasquini, L. 2011, *A&A*, **535**, A75
- Spitaleri, C. 1990, in *Problems of Fundamental Modern Physics*, ed. R. Cherubini, P. Dalpiaz & B. Minetti (2nd ed., Singapore: World Scientific)
- Spitaleri, C., Aliotta, M., Cherubini, S., et al. 1999, *PhRvC*, **60**, 055802
- Spitaleri, C., Lamia, L., Puglia, S. M. R., et al. 2014, *PhRvC*, **90**, 035801
- Spitaleri, C., Mukhamedzhanov, A. M., Blokhintsev, L. D., et al. 2011, *PAN*, **74**, 1725
- Strieder, F., Rolfs, C., Spitaleri, C., & Corvisiero, P. 2001, *NW*, **88**, 461
- Talon, S., & Charbonnel, C. 2010, in IAU Symp. 268, *Light Elements in the Universe*, ed. C. Charbonnel et al. (Cambridge: Cambridge Univ. Press), 365
- Tognelli, E., Degl’Innocenti, S., Marucci, L. E., & Prada Moroni, P. G. 2015a, *PhLB*, **742**, 189
- Tognelli, E., Degl’Innocenti, S., & Prada Moroni, P. G. 2012, *A&A*, **548**, A41
- Tognelli, E., Prada Moroni, P. G., & Degl’Innocenti, S. 2011, *A&A*, **533**, A109
- Tognelli, E., Prada Moroni, P. G., & Degl’Innocenti, S. 2015b, *MNRAS*, **449**, 3741
- Tribble, R. E., Bertulani, C. A., La Cognata, M., Mukhamedzhanov, A. M., & Spitaleri, C. 2014, *RPPH*, **77**, 106901
- Tumino, A., Spartá, R., Spitaleri, C., et al. 2014, *ApJ*, **785**, 96
- Tumino, A., Spitaleri, C., Mukhamedzhanov, A. M., et al. 2011a, *PhLB*, **705**, 546
- Tumino, A., Spitaleri, C., & Mukhamedzhanov, A. M. 2011b, *PhLB*, **700**, 111
- Valle, G., Dell’Omodarme, M., Prada Moroni, P. G., & Degl’Innocenti, S. 2013a, *A&A*, **549**, A50
- Valle, G., Dell’Omodarme, M., Prada Moroni, P. G., & Degl’Innocenti, S. 2013b, *A&A*, **554**, A68
- Wen, Q.-G., Li, C.-B., Zhou, S.-H., et al. 2008, *PhRvC*, **78**, 035805
- Xu, Y., Takahashi, K., Goriely, S., et al. 2013, *NuPhA*, **918**, 61
- Zahnow, D., Rolfs, C., Schmidt, S., & Trautvetter, H. P. 1997, *ZPhyA*, **359**, 211